The Astrophysical Journal, 1004:33 (11pp), 2026 June 10 https://doi.org/10.3847/1538-4357/ae6dac

Combining Multispacecraft Observations of a Coronal Mass Ejection with Numerical Simulations. I. Data-driven Modeling with RIMAP

Ruggero Biondo[1], Giuseppe Prete[2], Federica Frassati[1], Alessandro Bemporad[1], Salvatore Mancuso[1], Giuseppe Nisticò[2], Paolo Pagano[3,4], Silvia Perri[2], Fabio Reale[3,4], Roberto Susino[1], and Gaetano Zimbardo[2]
[1] INAF-Turin Astrophysical Observatory, Italy; ruggero.biondo@inaf.it
[2] University of Calabria, Department of Physics, Italy
[3] University of Palermo, Department of Physics and Chemistry, Italy
[4] INAF-Palermo Astronomical Observatory, Italy
Received 2026 March 23; revised 2026 May 2; accepted 2026 May 12; published 2026 June 3

Abstract

We present a comprehensive investigation of the fast coronal mass ejection (CME) event of 2022 September 5 by combining remote sensing observations, in situ measurements, and numerical magnetohydrodynamic (MHD) simulations. The CME, one of the most energetic of the recent solar cycle, was observed by SOHO and STEREO-A in the corona and intercepted in situ by the Parker Solar Probe (PSP) at ∼0.07 au and Solar Orbiter at ∼0.71 au. Using multiviewpoint coronagraphic data, we reconstruct the 3D geometry and kinematics of the CME-driven shock, deriving its propagation speed, direction, and initial size. These results are used to constrain a data-driven MHD simulation based on the RIMAP framework, which incorporates realistic solar wind conditions reconstructed from PSP and WIND measurements. The simulation reproduces key features of the shock and CME evolution detected at PSP, with a good quantitative agreement. For the Solar Orbiter, the model captures qualitative features of the shock passage, but does not fully reproduce the detailed temporal evolution of the event. The analysis highlights the importance of ambient solar wind structure and CME geometry in shaping shock propagation and evolution. We find that a simple cone model is insufficient to explain the observed duration of the event, requiring the inclusion of a velocity "tail" in the CME profile. Our results demonstrate the capability of combining multispacecraft observations with data-constrained MHD modeling to investigate CME evolution across the inner heliosphere and provide critical inputs for understanding shock-driven particle acceleration in extreme solar events.

Unified Astronomy Thesaurus concepts: Solar wind (1534); Solar corona (1483); Solar coronal mass ejections (310); Interplanetary shocks (829)

Materials only available in the online version of record: animation

1. Introduction

On 2022 September 5, an impressive coronal mass ejection (CME) was observed in situ by the Parker Solar Probe (PSP) at about 0.07 au and by the Solar Orbiter at ∼0.71 au. This CME was also observed remotely by STEREO-A and SOHO at 1 au. This was one of the strongest events observed in the last three decades, with a CME speed of 2200 km s^{-1} in the outer corona and an estimated mass of 2×10^{16} g (E. Paouris et al. 2023). The CME was propagating from the Sun toward the opposite side of Earth, and both PSP and the Solar Orbiter were in favorable positions to carry out coordinated observations. PSP was close to its 13th perihelion when it was impacted by the CME-driven shock at a heliocentric distance of $\sim 15\,R_\odot$; the PSP heliocentric distance decreased to less than $13.5\,R_\odot$ during the CME transit. In this period, PSP/WISPR (A. Vourlidas et al. 2016) was looking west of the Sun and was able to image the plasma and magnetic structures flowing over PSP.[5]

These unprecedented observations represent an excellent opportunity to study the evolution of CMEs, associated shocks, and energy conversion processes, and have attracted considerable interest (e.g., E. Paouris et al. 2023; C. M. S. Cohen et al. 2024; A. Kouloumvakos et al. 2025; P. Riley et al. 2025). For instance, Y. D. Liu et al. (2024) used the SOHO/Large Angle and Spectrometric Coronagraph (LASCO) C2 (G. E. Brueckner et al. 1995) and the STEREO-A/COR2 coronagraphs (M. L. Kaiser et al. 2008) to describe the CME-driven shock front as a sphere expanding and moving outward, with a peak speed of 2900 ± 200 km s^{-1}. Considering the backside viewpoint of SOHO and STEREO-A, this value is consistent with the average speed of about 2500 km s^{-1} obtained by R. Patel et al. (2023) using PSP/WISPR observations. In addition, E. Paouris et al. (2023), besides a speed of 2200 km s^{-1}, determine an acceleration $a \simeq 247$ m s^{-2} in the range of distances 1.2–14 $R_\odot$ (see their Figure 4, top panel) by using EUVI, COR1, and COR2 images. Y. D. Liu et al. (2024) also consider the possibility of magnetic reconnection in the heliospheric current sheet (HCS), which occurs in the sub-Alfvénic solar wind (i.e., below the Alfvén point), thus allowing for the closing of the magnetic flux back into the corona.

On the other hand, in coronagraph images, the structure of the CME appears to be rather complex, with the possibility of more than one eruption being at the origin of this event (D. M. Long et al. 2023; R. Patel et al. 2023). In this

[5] See the movies at https://wispr.nrl.navy.mil/encounter13-summary and https://parkersolarprobe.jhuapl.edu/News-Center/Show-Article.php?articleID=192.

connection, O. M. Romeo et al. (2023) have analyzed the in situ magnetic-field data by PSP/FIELDS (S. Bale et al. 2016), which exhibit two main magnetic inversion lines, and white-light coronagraph images: they suggest that possibly two adjacent CMEs are making up the September 5 event, with the possibility of the first CME being concave in 3D. We note that concave CME shapes have been obtained by numerical simulations by L. Yang et al. (2023), with the concavity corresponding to the HCS and being more pronounced beyond $20\,R_{\odot}$ from the Sun.

The CME-driven shock was detected in situ by PSP at 0.07 au and by the Solar Orbiter at 0.71 au, and the shock properties were studied by D. Trotta et al. (2024). They find that both spacecraft were crossed by the eastern flank of the shock, with a nonradial normal shock. Moreover, the shock speed along the normal shock in the spacecraft rest frame decreases from 1520 km s^{-1} at PSP to 942 km s^{-1} at the Solar Orbiter. Conversely, the Alfvénic (magnetosonic) Mach number varies slightly from $M_{\rm A} \simeq 3.9$ ($M_f \simeq 3.8$) at PSP to $M_{\rm A} \simeq 3.8$ ($M_f \simeq 3.2$) at the Solar Orbiter. D. Trotta et al. (2024) find that the shock at the Solar Orbiter is more structured and irregular than it is at PSP. Upstream of the Solar Orbiter shock, some shocklets are observed, too, which are seen to correspond to more isotropic electron pitch angle distribution than in the surroundings. The properties of solar energetic particles (SEPs) in PSP, in particular protons and helium above 80 keV, have been studied by C. M. S. Cohen et al. (2024), where some intriguing features are reported, such as the inverse velocity dispersion of particles above 1 MeV and the marked drop in proton intensities in the shock passage. The inverse velocity dispersion has been addressed also by A. Kouloumvakos et al. (2025), Z. Ding et al. (2025), and X. Chen et al. (2025).

According to the measurements made by the Radio Frequency Spectrometer (RFS) subsystem (10.5 kHz–19.17 MHz; M. Pulupa et al. 2017) of the FIELDS instrument suite (S. Bale et al. 2016) on PSP, the event produced type III and type II radio emission, as also outlined by J. Mitchell et al. (2024). While type III emission identifies beams of suprathermal electrons traveling along open magnetic-field lines (accelerated at reconnection sites near the Sun's surface during flares), decametric type II radio emission represents the clearest signature of the outward propagation of CME-driven shocks in the interplanetary medium. In particular, the multiple slowly drifting emission bands observed for this event, starting at about 16:10 UT, are typical of wide and rapidly expanding global shocks, which can produce multiple emission bands attributable to distinct source regions associated with different portions of the global shock (S. Mancuso et al. 2019). In fact, the strength of fast-mode shocks in the corona can vary due to the uneven distribution of the coronal Alfvén speed, but is greatly enhanced in those parts of the wave front that encounter low-Alfvén speed structures such as streamers, as suggested by S. Mancuso & J. C. Raymond (2004).

The 2022 September 5 CME was also studied by means of numerical simulations by Z. Ding et al. (2024), who used the EUHFORIA code (J. Pomoell & S. Poedts 2018) and the iPATH code (J. Hu et al. 2018), and by P. Riley et al. (2025) using the sunRunner3D code. In particular, the EUHFORIA code is initialized by a CME cone model, and the simulation results are compared with the in situ Solar Orbiter observations, showing a good agreement. It is worth pointing out that the CME structure obtained by the simulation in the equatorial plane also exhibits a concave shape (Z. Ding et al. 2024), i.e., in the words of those authors, a two-peak shape: this is due to the interaction of the CME with a slow stream with high density ahead of the shock nose. In P. Riley et al. (2025) instead, the CME is reproduced by localized trapezoidal modulations in the speed, density, and magnetic field at the inner boundary. The sunRunner3D simulation reproduces the observed speed profile at the Solar Orbiter, but with a temporal delay estimated around 5.84 hr. According to its authors, this delay is caused by the model not reproducing correctly the actual upstream solar wind in which the CME propagated, underestimating its speed.

In this paper, we carry out a joint investigation of the September 5 CME and associated shock, by means of remote observations, numerical simulations, and an analysis of in situ data. The CME-driven shock front properties in the corona are obtained from a 3D reconstruction using SOHO, STEREO-A, and FSI/EUI data and an ellipsoidal model for the shock front. The 3D reconstruction is used to derive parameters for the CME propagation modeled using numerical simulations based on RIMAP. RIMAP starts from the detailed reconstruction of the background Parker spiral on the orbital plane and uses it to set up a time-dependent MHD simulation of the CME propagation with the PLUTO code (R. Biondo et al. 2021b, 2022). The objective of the RIMAP simulation is to trace the evolution of the CME in the interplanetary space, with the specific goal to derive the properties of the shock propagation and structure and to provide constraints to the connected acceleration and transport of energetic particles. In the accompanying paper, we consider the magnetic turbulence levels upstream and downstream of the shock and investigate the high-quality energetic particle data for this event from the Solar Orbiter/EPD instrument (J. Rodríguez-Pacheco et al. 2020) and the intriguing energetic particle spectral index, which is found to be larger than that predicted by diffusive shock acceleration (DSA) for the observed compression ratio.

2. Data Analysis

Coronal images taken from spacecraft at different locations allow us to perform a 3D geometry reconstruction of the CME-driven shock. During the event, STEREO-A/COR2, SOHO/LASCO C2, and FSI/EUI on board the Solar Orbiter mission were available for such an analysis (see spacecraft positions in Figure 1). The longitudinal separation angle between STEREO-A and SOHO/LASCO was 19.°15 and between SOHO/LASCO and the Solar Orbiter was 149.°3. In particular, FSI/EUI was used to identify the source region, while the other two instruments were used to track the CME-driven shock expansion. Benefiting from the advantageous relative geometry between FSI/EUI and STEREO-A/COR2, the source region of the event was identified as the decaying NOAA Active Region 13088. This region had remained visible from Earth until August 28, after which it reappeared from the vantage point of the Solar Orbiter as the spacecraft advanced in its orbit. On September 5, the region was situated at approximately 33°W and 27°S, as viewed by FSI/EUI.

Although the relative geometry between SOHO/LASCO and STEREO-A/COR2 can limit the accuracy of a full 3D reconstruction, the inclusion of FSI/EUI observations enabled us to infer and constrain the propagation direction and to reconstruct the expanding front within the time interval

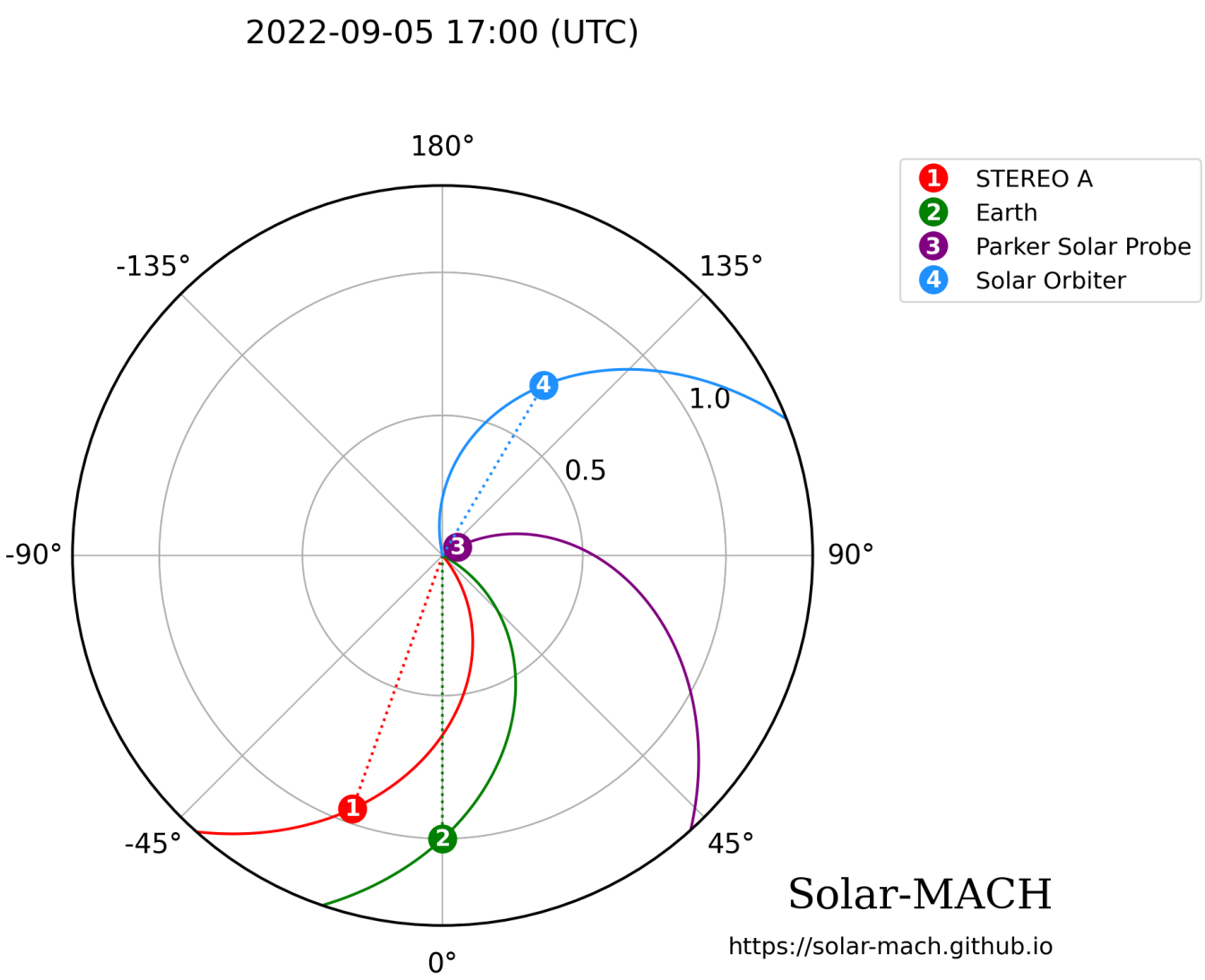

Figure 1. Positions of spacecraft during the event observations. The plot was built by using Solar-MACH (J. Gieseler et al. 2023) in Stonyhurst's coordinate system. The field lines are drawn by assuming a solar wind speed of 400 km s^{-1}, the mean value measured by in situ instruments on PSP and WIND before the shock arrival.

16:36–17:11 UT. Assuming that the propagation direction remained constant during this interval, the CME-driven shock geometry was subsequently recovered by fitting it with a spheroidal model (R.-Y. Kwon et al. 2014), characterized by the following key parameters: the height h of the spheroid, in units of solar radii ($R_\odot$), measured from the solar center; the self-similarity constant $\kappa = s/(h-1)$, where s is the azimuthal semiaxis of the spheroid; the eccentricity $e = \sqrt{1-q^2/s^2}$, for $s > q$ with $q = (h-1)/2$ as the radial axis. The wire-grid that best fits the expanding shock is shown in Figure 2 overplotted on the coronagraph images.

Using the 3D shock reconstruction, we determined the propagation direction of the backside event, which was oriented toward the southwest as viewed from Earth. The speed evolution along this trajectory was subsequently derived by fitting the distance–time profile (d–t) with a second-order polynomial. This results in an almost constant strong acceleration of $\sim$143 m s^{-2} (Figure 3), at least within the STEREO-A/COR2 field of view, and a velocity of $\sim$2150 km s^{-1} at $\sim$11.2$R_\odot$. While our velocity estimates appear consistent with those reported by E. Paouris et al. (2023), the derived acceleration is somewhat lower than their findings. This discrepancy is likely due to the fact that their analysis begins at approximately 1.3 $R_\odot$, a region where, statistically, CME acceleration tends to be more intense. Nonetheless, both results remain in agreement with the statistical trends presented by A. Ravishankar et al. (2020), who showed that fast CMEs ($v > 900$ km s^{-1}) typically reach their peak velocity within a heliocentric distance range of 5.5–10.5 $R_\odot$. Moreover, their maximum acceleration usually occurs within the first 2 hr after the CME onset, as also observed in the present case study. Our results were further compared with the analysis of A. Kouloumvakos et al. (2025), who adopted a similar approach. They estimated a maximum expansion velocity of $\sim$2480 $\pm$ 150 km s^{-1} around 16:46 UT, whereas our reconstruction yields a velocity of approximately 1950 km s^{-1} at the same time. In general, their values tend to be higher than those reported in other studies (O. M. Romeo et al. 2023; D. Trotta et al. 2024), a difference they attribute to possible factors such as the use of different measurement techniques (remote sensing versus in situ) and potential overestimation in the 3D speed reconstruction.

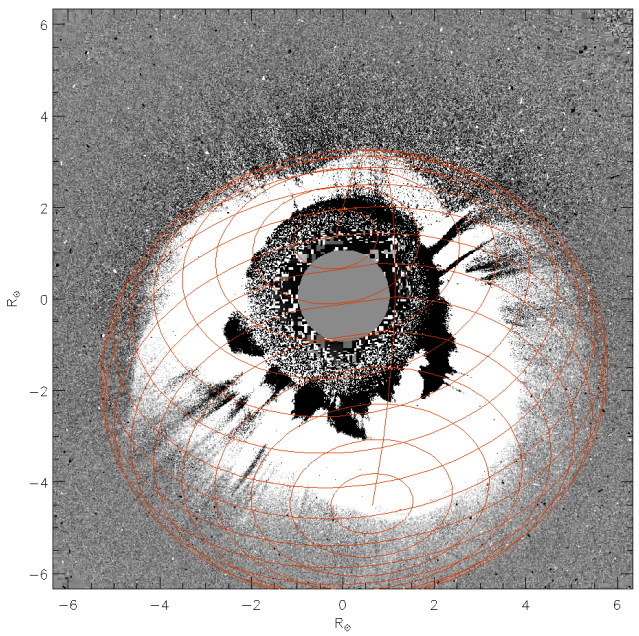

(a) STEREO-A/COR2.

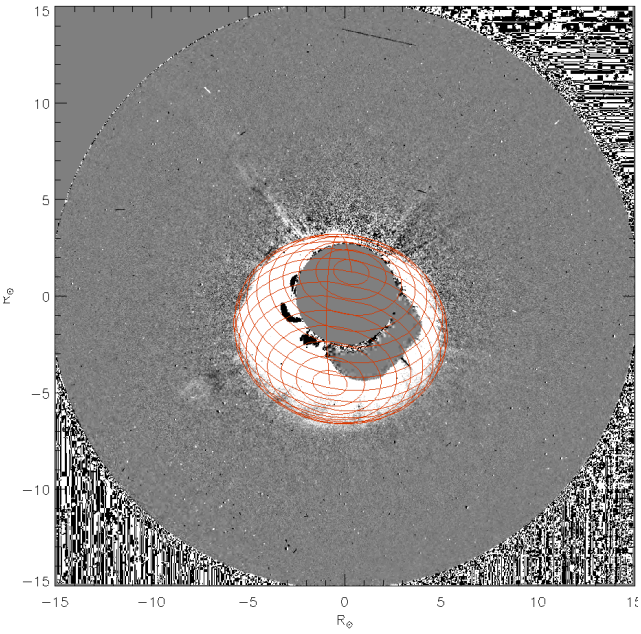

(b) LASCO-C2

Figure 2. The expanding shock front (identified with the red grid) as seen by STEREO-A/COR2 and LASCO-C2 at ∼16:46 UT. The images are running differences.

3. MHD Modeling

The data analysis in Section 2 allows us to set up a detailed numerical simulation of the CME propagation, using the Reverse In situ and MHD APproach (RIMAP; R. Biondo et al. 2021a). RIMAP is a hybrid ballistic-numerical method to reconstruct the plasma and magnetic-field conditions in the Parker spiral and bind them to in situ measurements. It uses data from spacecraft with heliocentric orbits as a primary input, back-mapping them to a chosen distance closer to the Sun. There, they become the boundary conditions of a numerical MHD simulation carried out with the PLUTO code (A. Mignone et al. 2007, 2012), which propagates these reconstructed solar wind streamlines until they fill the entire simulation domain. Then, these reconstructions can be used as a test bench to perform simulations of different models of solar transients (R. Biondo et al. 2021b, 2023). The main advantage of RIMAP is its high accuracy in reproducing solar wind and magnetic-field longitudinal structuring: the medium in which solar transients propagate is far from homogeneous, and the ambient condition of the heliosphere influences the propagation of SEPs (e.g., H. Q. He et al. 2011), and the interplanetary evolution of CMEs (B. Vršnak et al. 2013; M. Temmer & N. V. Nitta 2015).

Here, we use measurements of plasma and magnetic field collected by PSP from 2022 September 3 to 9, as an input for the reconstruction of the ambient condition, while the input CME parameters (in particular the initial cross-sectional radius and the propagation direction) derive from the 3D reconstruction discussed in Section 2. We choose this time interval of measurements because the PSP rotation around the Sun was faster than the Parker spiral one, and thus, any wind streamline is sampled only once. Starting from September 5 around 17:27, PSP passed through the CME, first encountering solar wind material perturbed by the CME (the interplanetary shock and its sheath), then material belonging to the proper CME (the magnetic flux rope) until September 6 (D. M. Long et al. 2023), and eventually returned to measure ambient solar wind.

Since we first want to reconstruct the ambient condition of the solar wind in which the perturbation propagated, we must remove the portion of measurements that we identified as transient and replace it with background values as realistic as possible. The identification of what constitutes CME material and what can instead be considered as background solar wind is complicated in this event by the simultaneous crossing of the HCS by PSP. Furthermore, even after the passage of the flux rope, around September 7, PSP experienced a dip in the solar wind mass flow rate. We choose to consider as background solar wind what PSP measured just before the encounter with the CME-driven shock, at 14:27 on September 5, and after 17:27 on September 9, when solar wind continuity returned to usual levels. The plasma and magnetic-field background data in the missing time window are replaced as follows. We use plasma measurements collected by the WIND spacecraft (R. Harten & K. Clark 1995), in order to obtain smooth profiles of the quantities in an ample portion of the Parker spiral, reflecting the large-scale trends in the considered time interval. Then, we map these profiles to the positions occupied by PSP during the missing time window. The radial magnetic-field polarity changes are placed where the joint analysis of magnetic helicity and the partial variance of increments (PVI; F. Pecora et al. 2021) found the discontinuities in the heliospheric magnetic-field direction (D. M. Long et al. 2023), assumed here to be crossings of the HCS.

The profiles of density, speed, pressure, and magnetic field spanning from 40 to 13 $R_\odot$ in distance are thus mapped back to 5 $R_\odot$ in distance, and then appropriately rescaled, building the inner boundary condition of the MHD simulation. The spherical grid used has 768 cells in the radial direction, 512 of them with uniform spacing from 5 to 60.5 solar radii and 256 stretched up to the outer boundary at 236.5 solar radii, and 1024 cells with uniform spacing in the longitudinal direction, with periodic boundary conditions. To ensure the solenoidality of the magnetic field, the divergence cleaning algorithm

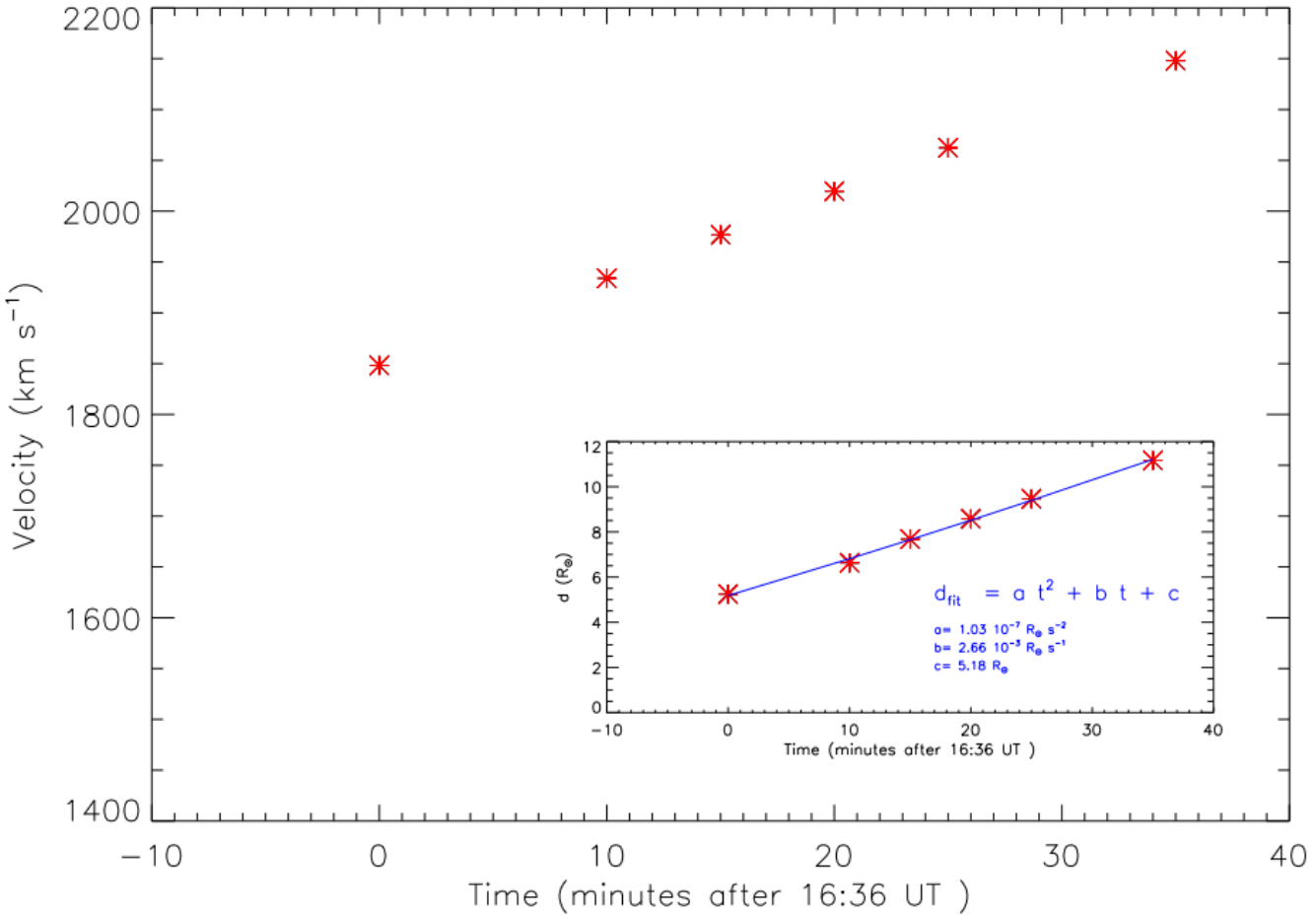

Figure 3. Speed evolution, along the propagation direction, inferred from the $d - t$ fitted profile (subplot). The event is characterized by an almost constant strong acceleration of $\sim$143 m s^{-2}.

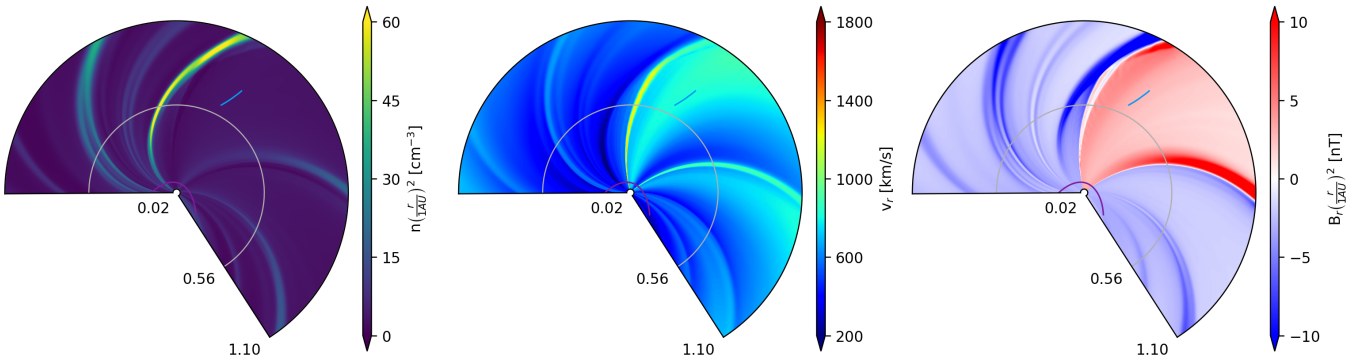

Figure 4. Equatorial maps of the interplanetary Parker spiral reconstructed by RIMAP, obtained starting from in situ measurements collected by Parker Solar Probe (PSP) from 2022 September 3 to September 10 (purple trajectory), close to the probe's 13th perihelion, and from WIND observations to fill the sliced portion of PSP data corresponding with the CME encounter. The azure line is the Solar Orbiter trajectory in the same time interval. From left to right, the maps of plasma density, radial velocity, and radial magnetic field are shown. A high-speed stream impacting on a low-speed stream and causing a corotating interaction region (CIR) is shown at the center right of the panels, around 0.8 au. Since the MHD equations are solved in a frame of reference corotating with the Sun, the CIR appears stationary.

(A. Dedner et al. 2002; A. Mignone et al. 2010) is used. Therefore, the ambient solar wind, obtained from the combination of PSP and WIND data, is allowed to relax into a stationary state, shown in Figure 4.

In this configuration, we build up the time-dependent 2D MHD simulation of the CME propagation with the PLUTO code. The CME is simulated starting from a modified cone model (e.g., H. Xie et al. 2004; J. Pomoell & S. Poedts 2018; R. Biondo et al. 2021b), the entrance into the inner radial boundary being described as a time-dependent boundary condition. The model assumes that the CME plasma propagates homogeneously before entering the simulation

Table 1
Initial Parameters for the Unmodified and Modified Cone Model CME Simulations Used in This Work

No.	Propagation Direction φ_0	Angular Width ω	Number Density $n_{\rm CME}$ (kg m^{-3})	Temperature $T_{\rm CME}$ (MK)	Bulk Speed $V_{\rm CME}$ (km s^{-1})	Tail Duration (hr)	Tail Function $f_{\rm tail}^{N.}$
0	57.5	80°	1.85 10^{-17}	2.0	2200	0.0	None
1	57.5	80°	1.85 10^{-17}	2.0	1700	7.6	linear
2	57.5	80°	1.85 10^{-17}	2.0	2200	7.6	Gaussian
3	57.5	80°	1.85 10^{-17}	2.0	2500	7.6	quartic exponential

Note. From $t = t_{\rm onset}$ onward for the cells within $\left[\varphi_0 - \frac{\omega}{2}; \varphi_0 + \frac{\omega}{2}\right]$, these values of velocity, number speed, and temperature are prescribed at the inner radial boundary instead of the background solar wind ones.

domain. The number density and plasma temperature inside the CME are also homogeneous. The kinematic parameters of the cone-modeled CME are derived from the shock reconstruction done in Section 2, which provided the angular width, bulk speed, and direction of propagation in the equatorial plane. The parameters used are summarized in Table 1. The CME as described by this cone model (#0) leads to a PSP encounter lasting less than 170 minutes. Instead, PSP traveled into the flank of the CME perturbation from September 5 17:30 UT to approximately September 6 02:00 UT. To better reproduce the measurements collected by PSP, we stretch the shape of the CME along the propagation direction by adding a speed "tail" to the original cone model. Here, we devise that the imposed plasma velocity linearly blends from the higher value of the homogeneous plasma bubble to the background solar wind during an interval of approximately 7.6 hr:

$$\boldsymbol{v}(5\,R_\odot,\,\varphi,\,t) = (1 - f_{\rm tail}\,(t))\;\boldsymbol{V}_{\rm background}(\varphi) + f_{\rm tail}\,(t)\;\boldsymbol{V}_{\rm CME} \tag{1}$$

where the time-dependent tail function $f_{\rm tail}$ is defined from the cone model parameter $t_{\rm half} = 5R_\odot \frac{\tan(0.5\,\omega)}{V_{\rm CME}} \approx 0.48$ hr. Different forms of $f_{\rm tail}$ can be used. In this work, we use these three:

$$f_{\rm tail}^{1}\,(t) = 1 - \left(\frac{t - t_{\rm half}}{16\,t_{\rm half}}\right) \tag{2}$$

$$f_{\rm tail}^{2}\,(t) = \exp\left[-\pi^2\left(\frac{t - t_{\rm half}}{16 t_{\rm half}}\right)^2\right] \tag{3}$$

$$f_{\rm tail}^{3}\,(t) = \exp\left[-\pi^4\left(\frac{t - t_{\rm half}}{16 t_{\rm half}}\right)^4\right] \tag{4}$$

as summarized in Table 1. For the first case, the initial value of the bulk speed is lowered from the 2200 km s^{-1} value estimated from Section 2 to 1700 km s^{-1}, in order to better capture the shock encounter at PSP. The second one uses the initial bulk speed of 2200 km s^{-1}, but the tail goes to zero faster than in the linear case, to follow the postshock plateau in PSP values. Finally, the third case uses the even higher speed estimated by A. Kouloumvakos et al. (2025), 2500 km s^{-1}, using an even faster tail.

Figure 5 shows two snapshots of the CME propagation across the RIMAP-reconstructed interplanetary Parker Spiral for case number 1. The first one, taken at 17:29 UT on September 5, covers the entire longitudinal domain and a distance from 0.02 to 0.11 au. The bottom one is taken at 14:57 UT on September 6, and spans from 0.02 to 0.88 au. From the left, contour maps of the number density, radial speed, and radial component of the magnetic field are shown. With our settings, the CME enters the computational domain on September 5, 06:14 UT as a homogeneous plasma cloud, with an isotropic expansion and a radial bulk velocity. Soon, the perturbation front is stretched and deformed, as it interacts with different streams of solar wind heterogenous in speed and density. The slow speed, high-density stream close to the first reversal of magnetic polarity drags the CME material more effectively than the fast, low-density ones found at the reversals, so that the resulting front profile shows two cusps.

On September 5, 17:29, the virtual PSP enters the CME by its eastern flank, marking the shock as shown by the top three panels of Figures 6 and 7. We compare the measured evolution of the density, velocity, and absolute magnitude of the magnetic field with the ones obtained from the MHD modeling. Figure 6 show the comparison between case #1 and the in situ measurements, while Figure 7 shows the comparison between the latter and all four simulations.

The encounter with PSP is marked by a sudden rise of all quantities at 17:29 UT. The density shows a sharp peak of a few minutes, up to less than 4000 cm^{-3}, while the velocity and the magnetic field decline more gradually than the steep increase to about 1300 km s^{-1} and 1600 nT, respectively, both decreasing linearly by about 50% in a couple of hours. While the density sharply returns to low values, even showing a relative void after 18:00 UT, both the velocity and the magnetic field settle to a plateau lasting longer for more than 6 hr, better defined in the velocity. After the void, the density shows a very irregular evolution, with several peaks and a long period of high values after 3:00 UT, which is not addressed in our modeling.

Our MHD model successfully reproduces several major features of the PSP encounter, both qualitatively and quantitatively. The timing of all quantities is matched very well, with the model showing a slight advance of a few minutes. Although broader, the model shows an overall similar peak of the density, with a good quantitative agreement to about 4000 cm^{-3}, and a plateau lower than the initial value after the peak. The velocity from the simulation has a very similar steep rise, and also shows a gradual linear decrease. Once ascertained that forcing the velocity tail at the perturbation entrance drives the decreasing trend, we decided not to pursue the details of this trend, which is shallower than the observed one in this case. Both the simulated and the observed magnetic field have a double peak at the encounter, the first being smaller than the second. The simulation main peak is lower than the observed one, below 1500 nT, and narrower in time, but the overall shape is remarkably similar.

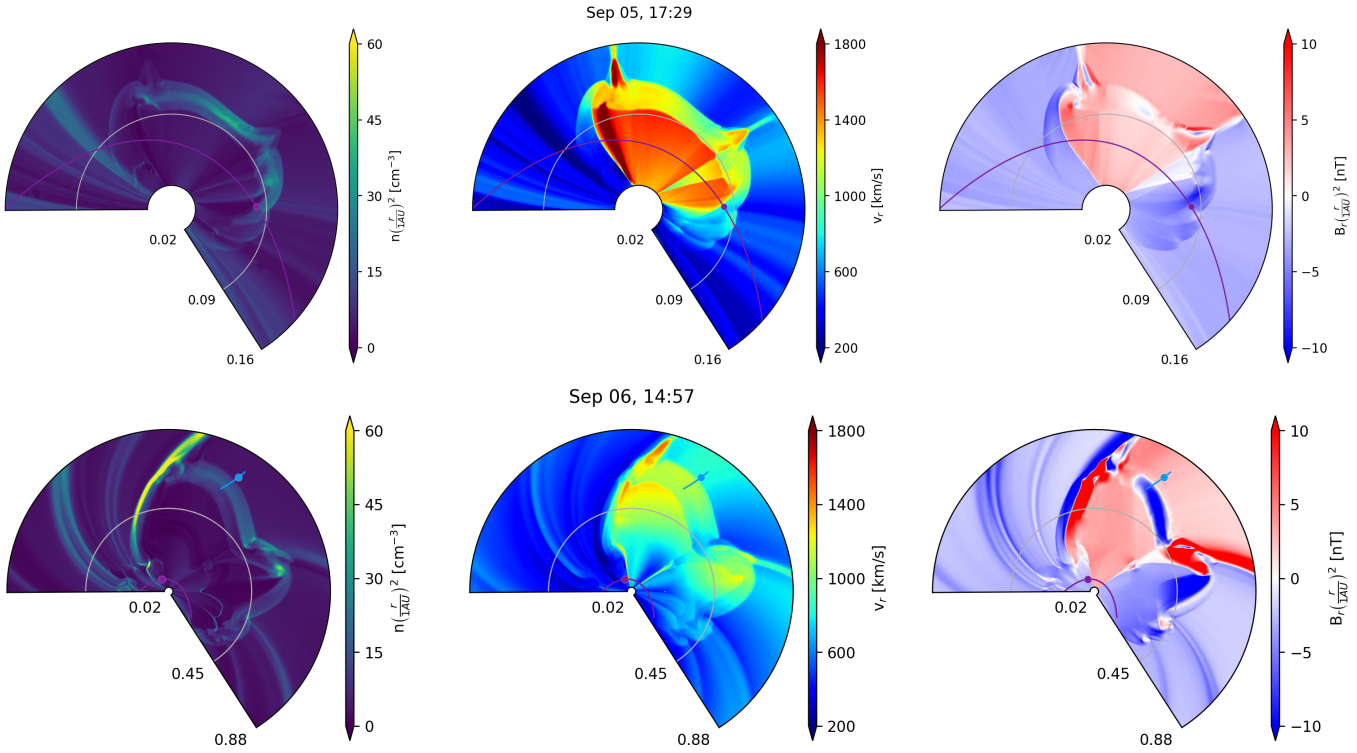

Figure 5. Equatorial maps of plasma density (on the left), radial speed (center), and radial magnetic field (right), showing two snapshots of the simulated CME propagating in the RIMAP-reconstructed interplanetary Parker spiral, for simulation #1. The purple dot marks the position of PSP along its orbit, represented by the purple line, while the azure dot and line indicate the Solar Orbiter. The top panels correspond to the simulated shock encounter at PSP on September 5, 17:29 UT, while the bottom panels correspond to the simulated shock encounter at the Solar Orbiter on September 6, 14:55 UT. The accompanying animation, available online, shows the simulation from September 5, 9:15 UT to September 8, 01:40 UT. It initially shows a close-up of the inner heliosphere, covering the radial range from 0.02 to 0.1 au, to follow the early CME evolution near PSP. As the CME propagates outward, the displayed radial extent is progressively enlarged to follow the expanding perturbation and keep the shock front visible. The animation eventually covers the full computational domain up to 1.1 au.
(An animation of this figure is available in the online article.)

The simulated field goes back to preencounter values. Due to the longitudinal inhomogeneity of the solar wind streamlines upstream and downstream, the quantity profiles display a degree of variation depending on the initial position of the virtual spacecraft, especially in the peak density at the shock. This effect becomes less important as we move far from the Sun, due to the spherical grid resolution.

In the simulation, the CME slows down to a speed slightly above 1000 km s^{-1} after crossing 0.1 au, and the perturbation front has piled up background solar wind density and compressed the field ahead. The CME front is detected by the Solar Orbiter at a distance of 0.71 au on September 6, at 10 UT (Figure 6, lower panels). The evolution of the measured quantities is somewhat different from that measured by PSP, due to both the interposed evolution and the different part of the CME intercepted by the Solar Orbiter. The density shows a very small and narrow, but equally well-defined, peak to about 20 cm^{-3}. Later, the density grows to even higher values (up to about 100 cm^{-3}) with a noisy trend, and stays there for several hours. A steep shock front is detected in the velocity to about 900 km s^{-1}, soon followed by another peak at about 1000 km s^{-1}. The velocity stays quite high above 600 km s^{-1}, with some modulation, and then decreases smoothly from 06:00 to 18:00 UT on September 7. The measured magnetic field has a sharp rise to about 40 nT at the encounter, with a very noisy evolution thereafter moving around this value, and with a final decline at about 09:00 UT on September 7.

In the simulation, the CME front reaches the Solar Orbiter around 15:25 UT, i.e., 5.5 hr after the measured shock encounter. Matching the timing and the relevant physical quantities of the encounters has been a particularly difficult task for this event. This is the case in which we could reproduce qualitatively most of the parameters at both spacecraft, at the expense of this time delay, which anyway appears as a reasonable compromise within a reasonable error bar. The simulated density at the Solar Orbiter does not show the small peak at the encounter, rather a steep rise of a shock front, followed by a more gradual rise around values very similar to the measured ones. Overall, also, the timescales are compatible with the measured density evolution. The simulated velocity shows the steep front to almost 900 km s^{-1} and then a long-lasting smooth high-speed state, which is overall similar to the observed trend, with a similar timescale and a similar very gradual decay to about 600 km s^{-1}. The magnetic field also shows a steep rise as the observed one, but it terminates into a well-defined bump with a width of about 6 hr and a peak of about 40 nT, a value not far from the measured field levels. The observed field enhancement lasts instead about 24 hr, which cannot be explained by the present model. Due to spherical grid geometry, the uncertainty on the spacecraft position has a negligible effect on the upstream and downstream profiles. However, it gives few minutes of uncertainty to the shock arrival time, as well as to its steepness.

Figure 7 shows a comparison of all of the four models listed in Table 1. They essentially differ for the initial values of CME

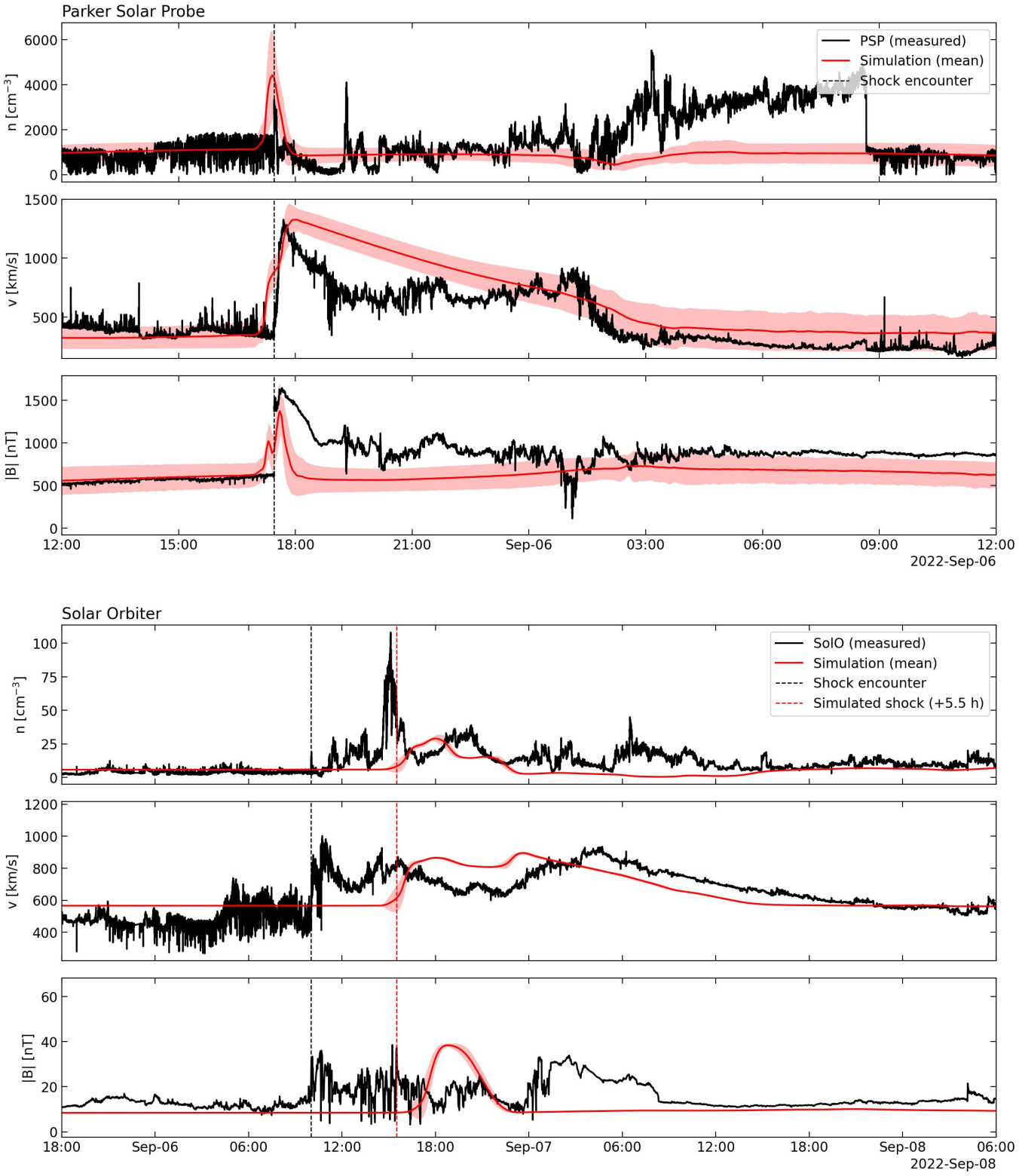

Figure 6. Time profiles of the number density, radial speed, and total magnetic field derived from the RIMAP MHD simulation (red) as compared to those measured by the Parker Solar Probe (PSP; top three panels) and Solar Orbiter (bottom panels). Dashed vertical lines mark the PSP shock encounter event at 17:27 UT on September 5 and those encountered by the Solar Orbiter at 10:01 UT on September 6. The dashed red line is the simulated shock encounter, experienced by the virtual SolO at 15:25, nearly 5.5 hr after the measured encounter. The transparent band surrounding the curve marks an uncertainty of 5° around the positions of the spacecraft.

bulk speed and shapes of the velocity tail. At the PSP encounter, they do not lead to substantial differences in the density and magnetic field. The unmodified cone model (#0) and the higher-speed model (#3) show a deeper void that better fits the data. There are instead remarkable differences in the velocity profile. The unmodified model top speed is

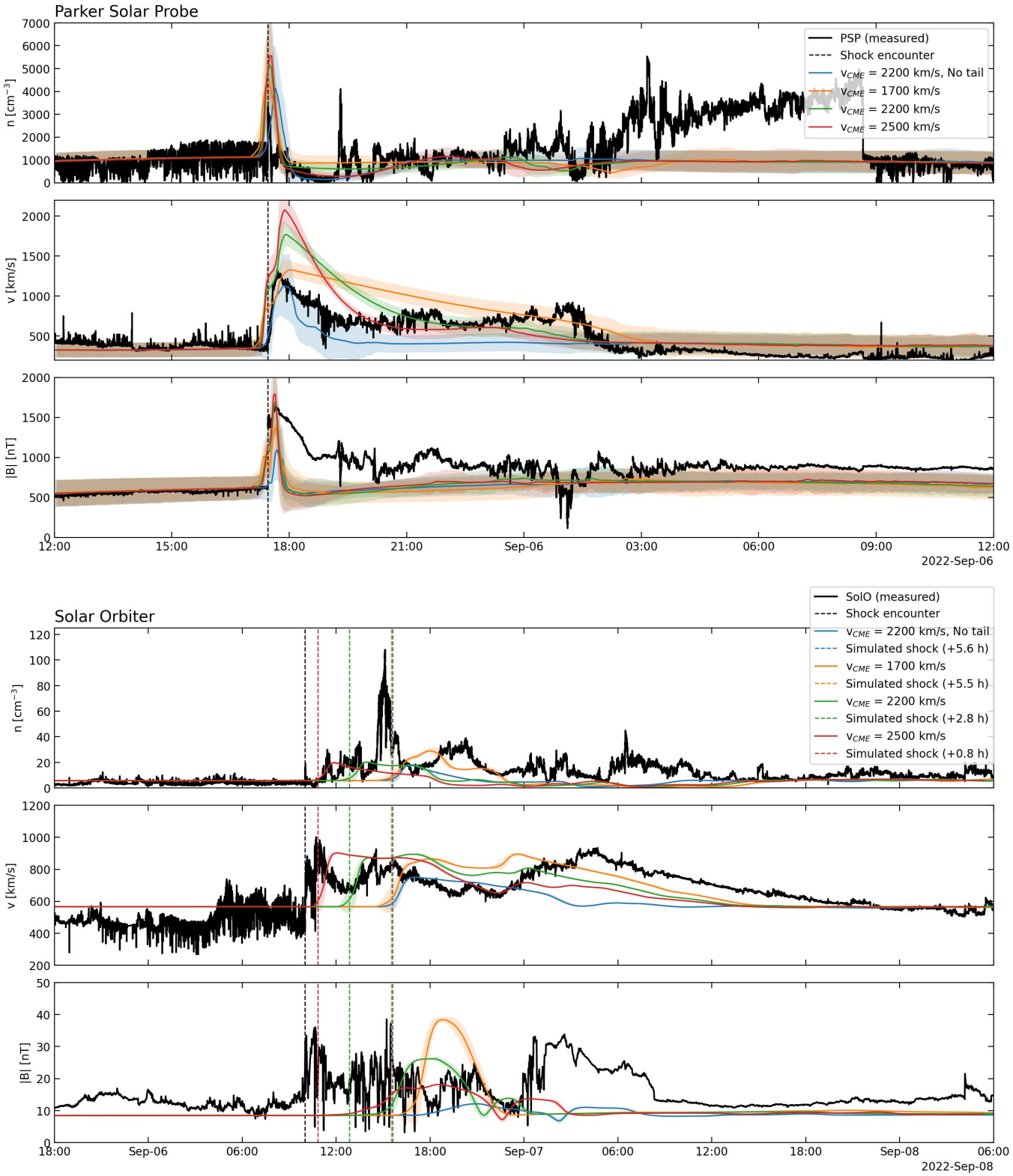

Figure 7. Same as Figure 6, with the addition of the other profiles made using the parameters reported in Table 1. Blue, orange, green, and red lines represent case 0, 1, 2, and 3, respectively. The bottom panels also show the different simulated shock encounter times, as experienced by the virtual Solar Orbiter 5.6, 5.5, 2.8, and 0.8 hr after the measured shock encounter at 10:01 UT on September 6.

slightly above 1000 km s^{-1}, and decreases to unperturbed values in less than 3 hr, way more rapidly than the measured event that lasted until September 6, 02:00 UT. Both the higher-speed models yield significantly higher velocities, almost to 2000 km s^{-1}, so model 1 definitely appears to provide the best matching. Regarding the Solar Orbiter encounter, higher-speed models lead to a lower density and magnetic-field values, while velocity values are comparable. The unmodified cone

model simulation shows a profile delay comparable to case #1, but with significantly less density and field compression, and with the top speed only reaching 750 km s^{-1}. The highest-speed model (#3) is the one that best matches the time of the encounter, with a delay of about 1 hr only. As explained above, however, this is the only real benefit of this choice, which makes us give a preference to the lower-speed model (#1).

As mentioned in the introduction, P. Riley et al. (2025) links their 5.8 hr delay with SolO shock to an underestimate of the upstream solar wind speed. However, in our 2D reconstruction, even an overestimate of the upstream speed leads to a similar, if smaller, time delay. It is possible that the inconsistency between the velocity measured by PSP at its shock encounter (less than 1500 km s^{-1}) and the time of the measured SolO shock (September 6, 10:01 UT) is due to the 3D geometry of the actual CME trajectory, which was directed southwest (as seen by Earth). While the Solar Orbiter was hit by the northern flank of the CME, far from its core, this is missed by our 2D simulation, where all the propagation and the interaction between the CME and the background wind happens on the equatorial plane. It is also likely that the absence of an inner full 3D magnetic structure of the CME may play a role in the shock delay, as well as in other discrepancies such as the duration of the encounter observed at SolO.

4. Conclusions

In this article, we carry out a coordinated investigation of the CME and associated shock event of 2022 September 5–6. This was one of the strongest events of the Solar Orbiter–PSP era. We have characterized the shock speed and acceleration in the solar extended corona by remote observations of SOHO and STEREO-A. The remote shock observations are used as an input for an MHD simulation of the heliospheric structure, based on RIMAP, a numerical approach that uses in situ measurements by PSP and other spacecraft to set up the solar wind where the CME propagates in greater detail. This allows a more detailed comparison with data measured in situ during the shock and CME passing.

The complexity of this event, likely composed of multiple coronal ejecta, together with the goal to make a comparison between two spacecraft located at very different heliocentric distances and sampling different portions of the CME-driven disturbance, makes our task particularly challenging. The model reproduces the PSP encounter quite accurately, capturing the shock arrival time, the order of magnitude of the density, velocity, and magnetic-field enhancements, and the overall shape of their early evolution. For the Solar Orbiter detection, the simulation captures several qualitative and quantitative aspects of the plasma profiles, including the velocity level and the compressed-density state, but it also shows a significant delay in the shock arrival and cannot reproduce the full duration of the magnetic-field enhancement.

Our attempt to match the in situ observations point by point through virtual spacecraft extracted along the trajectories of two different missions has been anyway successful for most of the quantities we had focused our model on (i.e., density and velocity of the CME front at either encounter). It is remarkable that a specific modeling of the CME density and velocity insertion profile is required to match the spacecraft observations, as in our case we had to adjust the standard CME cone model. To further improve the agreement between the simulated encounter profiles and PSP and Solar Orbiter data, it would be required to detail even more the inserted CME. This emphasizes how a simple standard CME model is effective for the simplicity of MHD models but falls short for detailing specific events, and that to use improved and more complex CME models is crucial for more accurate reconstructions in heliospheric models.

The model parameters are constrained by background wind and CME 3D reconstruction and imply a most likely initial speed of 1700 km s^{-1} and the necessity of a speed tail to explain the detected duration of the event larger than predicted by the simple cone model alone. Our reconstruction relies on a set of simplifying assumptions that define the scope of the model and should be considered when interpreting the detailed timing and morphology of the simulated in situ profiles. First, the simulation is restricted to the 2D equatorial plane, whereas the CME propagated slightly southwest. Therefore, the actual Solar Orbiter encounter, likely occurring at the northern flank of the disturbance, cannot be exactly reproduced in our model. This limitation may contribute to the time delay between the observed and simulated shock arrivals at the Solar Orbiter, as well as to differences in the duration and morphology of the simulated profiles. Second, the CME is described through a modified cone model, and thus does not include an internal magnetic structure of the ejecta, such as a flux-rope topology. As a consequence, the model is not expected to reproduce the detailed magnetic-field rotation and the full magnetic signatures observed in situ. Third, the background solar wind reconstruction made by RIMAP relies on a cutting/paste of data during the time interval of the CME passage in the PSP measurements, using WIND data and interpolation assumptions to recover the ambient solar wind. This may also affect the propagation speed, deformation, and compression of the modeled CME-driven shock. These limitations likely explain part of the remaining discrepancies, especially at the Solar Orbiter encounter, whose exact time depends on both the CME speed and the front morphology, although it is to be remarked that the comparison of both spatial and temporal features is an extremely challenging task for any modeling. A fully 3D description is expected to provide better results, but the parameter exploration becomes much more demanding. For instance, P. Riley et al. (2025) employed the 3D sunRunner3D model, but did not embed virtual spacecraft because of the large storage requirements, an issue that is avoided by the 2D nature of RIMAP. Their inner boundary at 19 $R_\odot$ also leaves the PSP encounter outside the simulation domain, while our reconstruction captures earlier phases of the propagation. Both sunRunner3D and RIMAP show a comparable delay, above 5 hr, between the observed and simulated shock encounters with the Solar Orbiter, despite the former underestimating and the latter overestimating the upstream solar wind speed. This suggests that the Solar Orbiter timing discrepancy cannot be explained only by the background solar wind speed and that the complex eruption configuration likely plays an important role. In this respect, the present work complements previous modeling efforts by extending the comparison down to the PSP perihelion distance and by using a background solar wind reconstruction directly constrained by in situ measurements. This allows us to test how the structured ambient wind influences the CME front already in the innermost heliosphere and to show that a modified injection profile is required to reproduce the duration of the PSP encounter. Moreover, our

modeling provides useful constraints for the subsequent analysis of this event.

In the framework of the whole investigation of this paper series, our modeling allows us to provide an accurate prediction regarding the shock compression ratio to be used for further analysis. From the simulation, we obtain that the shock compression ratio from PSP to the Solar Orbiter ranges from 2.2 to 3, higher than the values estimated for the same event by D. Trotta et al. (2024) from in situ measurements and similar to that found by Z. Ding et al. (2024) with the EUHFORIA MHD simulations. This will be the basis for the analysis of the shock-accelerated particles detected at the Solar Orbiter that is the subject of the accompanying article.

Acknowledgments

The authors acknowledge support by the Italian PRIN 2022, project 2022294WNB entitled "Heliospheric shocks and space weather: from multispacecraft observations to numerical modeling," funded by Next Generation EU, within Piano Nazionale di Ripresa e Resilienza (PNRR), Missione 4 "Istruzione e Ricerca"—Componente C2 Investimento 1.1, "Fondo per il Programma Nazionale di Ricerca e Progetti di Rilevante Interesse Nazionale (PRIN)," CUP H53D23000900006, CUP C53D23000820006, and CUP B53D23004760006. S.P., G.N., and G.Z. acknowledge the project "Data-based predictions of solar energetic particle arrival to the Earth: ensuring space data and technology integrity from hazardous solar activity events," "Finanziato dall'Unione europea—Next Generation EU" PIANO NAZIONALE DI RIPRESA E RESILIENZA (PNRR) Missione 4 "Istruzione e Ricerca"—Componente C2 Investimento 1.1, "Fondo per il Programma Nazionale di Ricerca e Progetti di Rilevante Interesse Nazionale (PRIN)," CUP H53D23011020001, Settore PE09. S.P., G.N., and G.Z. were further supported by the Space It Up project funded by the Italian Space Agency, ASI, and the Ministry of University and Research, MUR, under contract No. 2024-5-E.0—CUP No. I53D24000060005. F.F. acknowledges support from INAF grant CUP C63C23000810005 "IDEA-SW—Integrating Data and to Advance Space Weather forecasting of Catastrophic Events" and from the Project "Supporto per la realizzazione degli strumenti Metis, SWA DPU e STIX" CUP F86C18000570005. Computations were performed on the MEUSA cluster at the SCAN (Sistema di Calcolo per l'Astrofisica Numerica) facility for high-performance computing at INAF-Palermo Astronomical Observatory.

ORCID iDs

Ruggero Biondo https://orcid.org/0000-0002-3929-016X
Giuseppe Prete https://orcid.org/0000-0003-3739-3170
Federica Frassati https://orcid.org/0000-0001-9014-614X
Alessandro Bemporad https://orcid.org/0000-0001-5796-5653
Salvatore Mancuso https://orcid.org/0000-0002-9874-2234
Giuseppe Nisticò https://orcid.org/0000-0003-2566-2820
Paolo Pagano https://orcid.org/0000-0001-5274-515X
Silvia Perri https://orcid.org/0000-0002-8399-3268
Fabio Reale https://orcid.org/0000-0002-1820-4824
Roberto Susino https://orcid.org/0000-0002-1017-7163
Gaetano Zimbardo https://orcid.org/0000-0002-9207-2647

References

Bale, S., Goetz, K., Harvey, P., et al. 2016, SSRv, 204, 49
Biondo, R., Bemporad, A., Mignone, A., & Reale, F. 2021a, JSWSC, 11, 7
Biondo, R., Bemporad, A., Pagano, P., & Reale, F. 2023, A&A, 679, L14
Biondo, R., Bemporad, A., Pagano, P., et al. 2022, A&A, 668, A144
Biondo, R., Pagano, P., Reale, F., & Bemporad, A. 2021b, A&A, 654, L3
Brueckner, G. E., Howard, R. A., Koomen, M. J., et al. 1995, SoPh, 162, 357
Chen, X., Zhao, L., Giacalone, J., et al. 2025, ApJ, 994, 242242
Cohen, C. M. S., Leske, R. A., Christian, E. R., et al. 2024, ApJ, 966, 148
Dedner, A., Kemm, F., Kröner, D., et al. 2002, JCoPh, 175, 645
Ding, Z., Li, G., Mason, G., et al. 2024, A&A, 681, A92
Ding, Z., Wimmer-Schweingruber, R. F., Kollhoff, A., et al. 2025, A&A, 696, A199
Gieseler, J., Dresing, N., Palmroos, C., et al. 2023, FrASS, 9, 384
Harten, R., & Clark, K. 1995, SSRv, 71, 23
He, H. Q., Qin, G., & Zhang, M. 2011, ApJ, 734, 74
Hu, J., Li, G., Fu, S., Zank, G., & Ao, X. 2018, ApJL, 854, L19
Kaiser, M. L., Kucera, T. A., Davila, J. M., et al. 2008, SSRv, 136, 5
Kouloumvakos, A., Wijsen, N., Jebaraj, I. C., et al. 2025, ApJ, 979, 100
Kwon, R.-Y., Zhang, J., & Olmedo, O. 2014, ApJ, 794, 148
Liu, Y. D., Zhu, B., Ran, H., et al. 2024, ApJ, 963, 85
Long, D. M., Green, L. M., Pecora, F., et al. 2023, ApJ, 955, 152
Mancuso, S., Frassati, F., Bemporad, A., & Barghini, D. 2019, A&A, 624, L2
Mancuso, S., & Raymond, J. C. 2004, A&A, 413, 363
Mignone, A., Bodo, G., Massaglia, S., et al. 2007, ApJS, 170, 228
Mignone, A., Tzeferacos, P., & Bodo, G. 2010, JCoPh, 229, 5896
Mignone, A., Zanni, C., Tzeferacos, P., et al. 2012, ApJS, 198, 7
Mitchell, J., de Nolfo, G., Christian, E., et al. 2024, ApJ, 968, 33
Paouris, E., Vourlidas, A., Kouloumvakos, A., et al. 2023, ApJ, 956, 58
Patel, R., West, M. J., Seaton, D. B., et al. 2023, ApJL, 955, L1
Pecora, F., Servidio, S., Greco, A., & Matthaeus, W. H. 2021, A&A, 650, A20
Pomoell, J., & Poedts, S. 2018, JSWSC, 8, A35
Pulupa, M., Bale, S., Bonnell, J., et al. 2017, JGRA, 122, 2836
Ravishankar, A., Michałek, G., & Yashiro, S. 2020, A&A, 639, A68
Riley, P., Ben-Nun, M., González-Avilés, J. J., et al. 2025, JSWSC, 15, 17
Rodríguez-Pacheco, J., Wimmer-Schweingruber, R. F., Mason, G. M., et al. 2020, A&A, 642, A7
Romeo, O. M., Braga, C. R., Badman, S. T., et al. 2023, ApJ, 954, 168
Temmer, M., & Nitta, N. V. 2015, SoPh, 290, 919
Trotta, D., Larosa, A., Nicolaou, G., et al. 2024, ApJ, 962, 147
Vourlidas, A., Howard, R. A., Plunkett, S. P., et al. 2016, SSRv, 204, 83
Vršnak, B., Žic, T., Vrbanec, D., et al. 2013, SoPh, 285, 295
Xie, H., Ofman, L., & Lawrence, G. 2004, JGRA, 109, A03109
Yang, L., Hou, C., Feng, X., et al. 2023, ApJ, 942, 65